

See discussions, stats, and author profiles for this publication at: <https://www.researchgate.net/publication/256842767>

On the state of Pd in methane oxidation catalysts of composition $A(B,Pd)O_{3\pm\delta}$ (A=La, Y; B=Mn, Fe, Co)

ARTICLE in CHEMISTRY OF MATERIALS · JANUARY 2012

Impact Factor: 8.35

READS

38

8 AUTHORS, INCLUDING:



Maarten Nachtegaal

Paul Scherrer Institut

105 PUBLICATIONS 1,343 CITATIONS

SEE PROFILE



Santhosh Kumar Matam

Empa - Swiss Federal Laboratories for Materia...

66 PUBLICATIONS 1,245 CITATIONS

SEE PROFILE



Anke Weidenkaff

Universität Stuttgart

294 PUBLICATIONS 3,466 CITATIONS

SEE PROFILE



Davide Ferri

Paul Scherrer Institut

133 PUBLICATIONS 2,682 CITATIONS

SEE PROFILE

On the State of Pd in Perovskite-Type Oxidation Catalysts of Composition $A(B,Pd)O_{3\pm\delta}$ ($A = La, Y$; $B = Mn, Fe, Co$)[†]

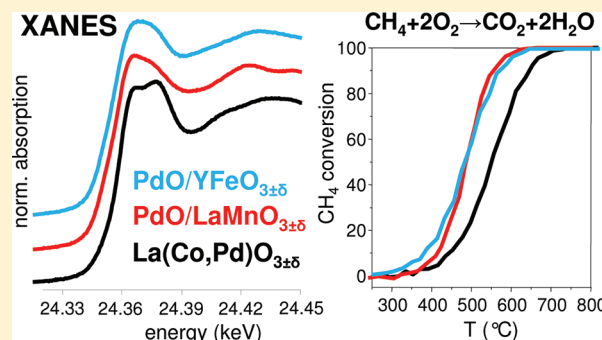
Arnim Eyssler,[‡] Alexander Winkler,^{§,⊥} Olga Safonova,^{||} Maarten Nachtegaal,^{||} Santhosh Kumar Matam,[‡] Paul Hug,[‡] Anke Weidenkaff,[‡] and Davide Ferri^{‡,*}

[†]Laboratory for Solid State Chemistry and Catalysis and [§]Internal Combustion Engines Laboratory, Swiss Federal Laboratories for Materials Science and Technology, Empa, Ueberlandstrasse 129, CH-8600 Dübendorf, Switzerland

^{||}Paul Scherrer Institute, CH-5232 Villigen, Switzerland

ABSTRACT: Incorporation of palladium within the perovskite-type lattice is a valuable strategy to prevent sintering phenomena that reduce the performance of automotive catalysts. However, occupation of B-site coordination sites by Pd can strongly depend on the nature of the perovskite-type oxide and care must be taken for structural interpretation. Pd-based $La(B,Pd)O_{3\pm\delta}$ ($B = Mn, Fe, Co$) perovskite-type oxides and $Y(Fe,Pd)O_{3\pm\delta}$ have been prepared by the amorphous citrate method by introducing the Pd salt to the precursors solution with the aim to substitute the B-site. The state of Pd was thoroughly characterized using X-ray absorption spectroscopy, X-ray photoelectron spectroscopy, and temperature-programmed reduction with hydrogen. Pd incorporation was achieved for $La(Fe,Pd)O_{3\pm\delta}$ and $La(Co,Pd)O_{3\pm\delta}$ that showed the XANES white line of Pd in octahedral coordination. On the contrary, $La(Mn,Pd)O_{3\pm\delta}$ showed XANES features and reduction behavior typical of segregated PdO particles. The state of Pd in $Y(Fe,Pd)O_{3\pm\delta}$ appeared to be dependent on the calcination temperature. Calcination at 700 °C produced cationic palladium with strong interaction with the $YFeO_3$ structure but likely in a different coordination environment than in $LaFeO_3$. Calcination at 800 °C provided improved crystallinity and forced Pd to form a PdO phase. The markedly different states of Pd are interpreted on the base of ionic radii arguments. The smaller size of Mn cations does not favor occupation of octahedral sites by the larger Pd^{3+} . The observed states adopted by Pd strongly influenced methane oxidation activity. The highest catalytic activity was found for the samples where palladium was predominantly dispersed as supported PdO particles. Lowest catalytic activity was measured for samples containing octahedral Pd, thus confirming that Pd incorporation in the perovskite-type lattice may not be favorable for methane oxidation.

KEYWORDS: palladium, perovskite-type oxides, methane oxidation, coordination state



1. INTRODUCTION

The A- and B-site cations of perovskite-type oxides of general formula ABO_3 can be partly substituted to generate a vast range of functional materials whose properties can be tailored according to the application, including fuel cell cathodes and anodes,¹ catalysts,^{2,3} photocatalysts,^{4,5} and thermoelectric materials.⁶ Perovskite-type oxides have been reported since the 1970s as oxidation catalysts and represent a valid alternative to automotive emission control catalysts based on precious metals. The interest for perovskite-type oxides in the field has been renewed by the observation that some formulations^{7,8} enable precious metal atoms to reversibly segregate out of and reintegrate into the perovskite lattice under reductive and oxidative atmosphere, respectively. This “self-regenerating property” is capable of limiting precious metal particle sintering under periodic redox fluctuations of the feedstock, like in the case of catalysts used for exhaust after treatment of stoichiometric engines. Similarly, it was earlier realized that perovskite-type oxides could be used as precursors of supported

metal catalysts by exploitation of the segregation of metallic particles upon reduction.^{2,9,10}

Various works report on the synthesis, characterization, and catalytic properties of perovskite-type oxides with substitution of the B-site cation by Pd. In their pioneering work, the group at Daihatsu^{7,11} prepared $La(Fe,Co,Pd)O_3$ and $La(Fe,Pd)O_3$ by the alkoxide method and studied the origin of their three-way catalytic activity using mainly X-ray absorption spectroscopy (XAS) and X-ray photoelectron spectroscopy (XPS). The oxidation and coordination states of Pd were analyzed after reduction and reoxidation of catalysts in a wide temperature range. The shift of the Pd K-edge energy justified the interpretation that reduction and successive reoxidation at constant temperature induce reversible structural changes related to the periodic segregation and reincorporation of Pd out of and into the perovskite-type structure. XPS confirmed that the oxidation state of Pd changes reversibly between Pd^0

Received: February 21, 2012

Published: April 25, 2012



and the unusually high oxidation state Pd^{3+} , corresponding to palladium in solid solution with the perovskite lattice.¹¹ Such a high valence state of palladium is considered crucial for low temperature catalysis.¹² A useful scale for the formation of Pd-, Pt-, and Rh-perovskite solid solutions was provided for various perovskite-type oxides, including LaAlO_3 , BaZrO_3 , CaTiO_3 , BaTiO_3 , SrTiO_3 , and SrZrO_3 .⁸

In addition to the shift of the Pd K-edge energy compared to Pd^{2+} in PdO, a doublet at the white line was considered the fingerprint of cationic palladium in the distorted octahedral coordination of $\text{LaFe}_{0.95}\text{Pd}_{0.05}\text{O}_{3\pm\delta}$ prepared by the amorphous citrate method.^{13,14} XAS and electron paramagnetic resonance (EPR) were used to demonstrate that Pd in flame made 0.5 wt % Pd- $\text{LaCoO}_{3\pm\delta}$ had been incorporated within LaCoO_3 . However, the Pd white line significantly differed from that of $\text{LaFe}_{0.95}\text{Pd}_{0.05}\text{O}_{3\pm\delta}$.¹³ $\text{La}(\text{Fe,Pd})\text{O}_{3\pm\delta}$ prepared by ultrasonic spray combustion (USC) evidenced the formation of the Pd- LaFeO_3 solid solution that was confirmed by the same XANES fingerprint.¹⁵ On the contrary, $\text{La}(\text{Mn,Pd})\text{O}_3$ prepared by a wet chemistry route did not exhibit the same white line shape but rather that of PdO in supported Pd catalysts. The dual site Pd- LaMnO_3 catalyst prepared by the solution combustion method has the property to activate incorporated palladium by its reduction and segregation out of the LaMnO_3 lattice upon treatment at temperatures above the threshold temperature of PdO_x decomposition.¹⁶ XPS showed that Pd is present predominantly as Pd^{2+} ; however, a fraction of Pd^{4+} strongly interacting with the perovskite structure was also observed. Similarly, platinum group metals in $\text{La}(\text{Mn,PGM})\text{O}_3$ (PGM = Pd, Pt, Rh) have shown strong interaction with the perovskite structure by H_2 -TPR and O_2 -TPD.¹⁷ Pd in SrFeO_x exhibited a stronger white line feature than that of PdO, therefore underlying the strong degree of interaction responsible for the improved exhaust emission control properties.¹⁸

The state of Pd was thoroughly characterized in the case of two formulations. Pd^{2+} in the $\text{BaCe}_{1-x}\text{Pd}_x\text{O}_3$ exhibits an oxygen-deficient square-planar coordination not reported before for Pd in a perovskite-type structure.¹² XANES data showed an anomalous white line shape at the Pd K-edge, with respect to that of dispersed PdO catalysts and of $\text{LaFe}_{0.95}\text{Pd}_{0.05}\text{O}_3$ and in this sense representing novel surface truncated square pyramidal PdO_5 species characterized by unusual coordination geometry of the palladium site adjacent to an oxygen vacancy. The material demonstrated high CO oxidation activity that was attributed to the presence of this species.¹⁹ Since the missing surface oxygen coordination site in this structure can be reversibly replenished by gas phase oxygen under oxygen rich conditions, the “ingress and egress” mechanism resembles that proposed by DFT simulation considering that the self-regenerative function originates from oxygen mobility rather than from the mobility of Pd.²⁰ Further, $\text{YFe}_{1-x}\text{Pd}_x\text{O}_{3-\delta}$ tested for CO oxidation exhibits the same self-regenerative property of perovskite-type oxides.²¹ In this case, Pd^{2+} occupies the Fe sites in 5-fold coordination and contributes to the stabilization of the hexagonal structure.

These studies demonstrate that Pd can in principle adapt to the crystal structure of the host lattice and therefore adopt various coordination environments. We shall show here that this might depend on the nature of the host structure in the case of lanthanum-based perovskite-type oxide oxidation catalysts containing Mn, Fe, or Co.²² In this work we investigate the substitution of Pd at the B-site of perovskite-type LaBO_3 (B = Mn, Fe, Co) and of the perovskite-related

YFeO_3 using a range of characterization techniques aiming at identifying the state of the catalytically active Pd phase as a function of the nature of the B-site cation and of the bulk structure. Methane oxidation is used to probe the catalytic properties of the oxidation state and coordination environment of Pd in these samples.

2. EXPERIMENTAL SECTION

2.1. Catalyst Preparation. Pd-containing perovskite-type catalysts of the formula $\text{LaB}_{0.95}\text{Pd}_{0.05}\text{O}_{3\pm\delta}$ (B = Mn, Fe, Co) and hexagonal $\text{YFe}_{0.95}\text{Pd}_{0.05}\text{O}_3$ were prepared by the amorphous citrate method.²³ Aqueous solutions of the metal nitrates ($\text{La}(\text{NO}_3)_3 \cdot 6\text{H}_2\text{O}$ (puriss. > 99%, Fluka), $\text{Fe}(\text{NO}_3)_3 \cdot x\text{H}_2\text{O}$ ($x = 7.5$, estimated by TGA; 98+%, A.C.S., Sigma-Aldrich), $\text{Co}(\text{NO}_3)_2 \cdot 6\text{H}_2\text{O}$ (>97%, Merck), $\text{Mn}(\text{NO}_3)_2 \cdot 4\text{H}_2\text{O}$ (98%, Alfa Aesar), $\text{Y}(\text{NO}_3)_3 \cdot 6\text{H}_2\text{O}$ (99.9%, Alfa Aesar), and $\text{Pd}(\text{NO}_3)_2 \cdot 2\text{H}_2\text{O}$ (99.9%, Alfa Aesar) were mixed with an aqueous solution of citric acid (assay 99.5–100.5%, Riedel-de Haën) in a 1:1 molar ratio with respect to the sum of metal salts. The solvent was evaporated in a rotary evaporator (60 °C, 60 mbar) until a viscous product was obtained, which was then dried in a vacuum oven for 12 h (80 °C, 60–80 mbar). The obtained dry foam was crushed and calcined at 700 °C for 2 h in flowing synthetic air (99.995 vol %) at atmospheric pressure. The Y-containing sample was additionally calcined at 750 and 800 °C. The samples are denoted as $\text{La}(\text{Mn,Pd})\text{O}_3$, $\text{La}(\text{Fe,Pd})\text{O}_3$, $\text{La}(\text{Co,Pd})\text{O}_3$, $\text{Y}(\text{Fe,Pd})\text{O}_3$, $\text{Y}(\text{Fe,Pd})\text{O}_3$ -750, and $\text{Y}(\text{Fe,Pd})\text{O}_3$ -800. LaMnO_3 , LaFeO_3 , LaCoO_3 , YFeO_3 , and YFeO_3 -800 were prepared by the same synthesis route. A commercial 2 wt % Pd/ Al_2O_3 catalyst (kindly provided by Umicore; surface area, 135 m²/g; Pd dispersion, 20%) was used as a reference sample for XPS and XAS measurements.

2.2. Characterization. The palladium loading of the catalysts was determined by ICP-OES.¹³ The specific surface area (SSA) was determined with a Quantachrome CHEMBET 3000 instrument. Prior to the measurements, catalysts were pretreated in a nitrogen flow (25 mL/min) for 30 min at 200 °C to remove moisture and physisorbed species. The specific surface area was then determined from nitrogen adsorption at –196 °C using 30 vol % N_2/He and applying the single-point differential BET method. Hydrogen temperature programmed reduction (H_2 -TPR) was performed with the same Quantachrome CHEMBET 3000 instrument. Prior to TPR, all samples were calcined at 500 °C for 30 min in synthetic air (60 mL/min), cooled to room temperature, and flushed with nitrogen for 30 min at 200 °C to remove physisorbed oxygen. A quartz glass reactor was loaded with 100 mg sample powder, and a K-Type thermo couple was inserted into the middle of the catalyst bed. H_2 -TPR experiments in 5 vol % H_2/N_2 (25 mL/min) were performed in the temperature range –25 to 900 °C. The crystal structure and phase composition of the catalysts were determined by powder X-ray diffraction using an X'Pert Pro diffractometer (PANalytical) and Cu K α radiation ($\lambda = 1.5418 \text{ \AA}$).

Atomic concentrations and valence states of the surface elements were determined by X-ray photoelectron spectroscopy (XPS). Spectra were recorded with a Physical Electronics (PHI) Quantum 2000 photoelectron spectrometer using monochromatic Al K α radiation and a hemispherical capacitor electron-energy analyzer equipped with a channel plate and a position sensitive detector operating in the constant pass energy mode. Quantitative analysis was performed using Spectral Data Processor V4.3 and PHI MultiPak V6.1A. The C 1s signal position at the binding energy (BE) of 284.8 eV was used as an internal standard for calibration of the XP-signal positions.

X-ray absorption near-edge structure (XANES) and extended X-ray absorption fine structure (EXAFS) measurements were performed *ex situ* on sample pellets at the Pd K-edge (24.35 keV) in the transmission mode (monochromatic radiation, Si(311) double crystal) at beamline X1 at Hasylab (DESY, Hamburg, Germany). *In situ* XANES spectra were collected at the SuperXAS beamline at the Swiss Light Source (SLS, Villigen, Switzerland) in fluorescence mode using a germanium 13-element detector equipped with a Ni slit. The sample (50–70 mg, sieve fraction 0.1–0.15 mm) was firmly fixed between quartz wool plugs in quartz capillaries ($d_i = 2.8 \text{ mm}$, 0.1 mm wall

Table 1. Physico-Chemical Properties of the Catalysts

sample	T_{calc} (°C)	SSA (m ² /g)	Pd content				XRD
			(wt %) ^a	(mol) ^a	(at %) ^a	(at %) ^b	
La(Fe,Pd)O ₃	700	14	2.01 ± 0.01	0.0463	0.93	0.6	orthorhombic (<i>Pnma</i>) ³¹
La(Co,Pd)O ₃	700	9	1.90 ± 0.01	0.0442	0.88	0.5	rhombohedral (<i>R3c</i>) ⁶³
La(Mn,Pd)O ₃	700	12	1.86 ± 0.01	0.0435	0.87	1.3	rhombohedral (<i>R3c</i>) ²⁹
Y(Fe,Pd)O ₃	700	21	2.37 ± 0.01	0.0434	0.87	0.7	hexagonal, ²⁷ Fe ₂ O ₃ , Y ₂ O ₃
Y(Fe,Pd)O ₃ -800	800	10	2.37 ± 0.01	0.0434	0.87	1.2	hexagonal, ²⁷ Fe ₂ O ₃ , Y ₂ O ₃
LaFeO ₃	700	14					orthorhombic (<i>Pnma</i>) ³¹
LaCoO ₃	700	6					rhombohedral (<i>R3c</i>) ⁶³
LaMnO ₃	700	20					rhombohedral (<i>R3c</i>) ²⁹
YFeO ₃	700	23					hexagonal, ²⁷ Fe ₂ O ₃ , Y ₂ O ₃
YFeO ₃ -800	800	14					hexagonal, ²⁷ Fe ₂ O ₃ , Y ₂ O ₃

^aDetermined by ICP-OES. ^bDetermined by quantitative XPS analysis.

thickness, Hilgenberg).^{24,25} The capillaries were mounted in a sample holder with gas supply and sealed with Teflon fittings. Temperature programmed reduction was performed in the 25–600 °C temperature range in 5 vol % H₂/He (45 mL/min). All data processing, analysis, and plotting were carried out using IFEFFIT 1.2.11c.²⁶ The spectra were background-corrected and normalized by subtracting a linear fit and by dividing the post-edge region by a third-degree polynomial fit. The radial distribution function was obtained from Fourier transforming k^2 -weighted $\chi(k)$ data in the range of 1.5–12.8 Å⁻¹ using a Bessel window function.

2.3. Catalytic Oxidation of Methane. Catalytic activity measurements for the oxidation of methane were carried out in a quartz glass reactor ($d_i = 6$ mm) that was placed inside a vertical electrically heated tubular furnace. The reactor was loaded with 100 mg of catalyst (sieved fraction, 0.15–0.2 mm) that was mixed in the mass ratio 1:4 with sea sand (p.a., cleaned and calcined at 1000 °C, Roth GmbH) and firmly fixed between quartz wool plugs (bed length, 15 mm). The temperature was measured on top of the catalyst bed using a K-type thermocouple. Prior to reaction, the catalyst was activated in 20 vol % O₂/He (50 mL/min) at 500 °C for 2 h. After cooling to 200 °C the gas flow was changed to the reaction mixture (1 vol % CH₄/4.4 vol % O₂, balance He, 130 mL/min; GHSV = 18 400 h⁻¹). Methane oxidation was carried out in the 200–900 °C temperature range at a rate of 5 °C/min. The cooling rate strongly deviated from 5 °C/min below 600 °C; nevertheless, all samples experienced identical conditions thus allowing comparison within the cooling segment. The exhaust gas stream was monitored with a gas chromatograph (3000A micro GC, Agilent Technologies) equipped with PoraPlot-Q and molecular sieve 5 Å columns. GC data were treated with the EZChrom Elite software package. In all measurements, CO₂ and H₂O were the only detected products. Methane conversion is expressed as $X_{\%} = 100(\text{CH}_4^0 - \text{CH}_4^T)/\text{CH}_4^0$, where CH₄⁰ is the area of the GC peak of CH₄ at 200 °C and CH₄^T the area at a given temperature T .

3. RESULTS AND DISCUSSION

3.1. Physicochemical Properties. Table 1 demonstrates that the Pd-substituted samples exhibited Pd loadings between 1.86 and 2.37 wt %, which corresponds to 0.0435–0.0463 mol Pd. The specific surface area varied in the range 9–22 m²/g, the highest value being observed for Y(Fe,Pd)O₃, suggesting a smaller average particle size compared to the other samples. The Mn-containing sample experienced the largest variation of surface area upon addition of Pd, the value decreasing from 20 m²/g of LaMnO₃ to 12 m²/g of La(Mn,Pd)O₃.

Y(Fe,Pd)O₃ calcined at 700 °C displayed a diffraction pattern with few broad reflections indicating the poor crystallinity of the sample (Figure 1). The small and broad peaks at 2θ 30.3° (101) and 33.2° (102) were identified as the main peaks of the hexagonal phase.²⁷ The crystallinity of the sample improved manifestly after calcination at 750 and 800 °C

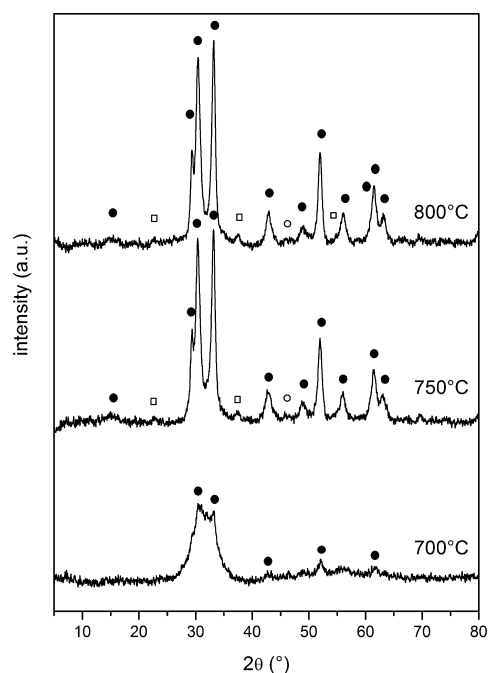


Figure 1. X-ray diffraction patterns of Y(Fe,Pd)O₃ calcined at different temperatures. Symbols: hexagonal phase (●) and Fe₂O₃ (□) and Y₂O₃ (○).

but Fe₂O₃ and Y₂O₃ were still detected, thus proving the difficulty to obtain pure phase YFeO₃ by the amorphous citrate method at these temperatures.^{21,28} Y(Fe,Pd)O₃ and Y(Fe,Pd)O₃-800 were used for further comparison with the other samples. Figure 2 compares the XRD pattern of Y(Fe,Pd)O₃-800 with those of the La(B,Pd)O₃ (B = Mn, Fe, Co) samples calcined at 700 °C. The rhombohedral La(Mn,Pd)O₃ and La(Co,Pd)O₃^{29,30} and the orthorhombic La(Fe,Pd)O₃³¹ crystal structures were identified. No secondary phases, including PdO, were detected in the perovskite-type oxides LaBO₃ and La(B,Pd)O₃. The absence of any reflection of the PdO phase is however not conclusive about the actual state of Pd. Moreover, the crystal structure of the Pd-free samples was identical to that of the doped samples shown in Figure 2 (Table 1). No appreciable shift of the perovskite-type reflections could be observed following addition of Pd that could have revealed occupation of the B-site by Pd. However, the characteristic doublet features typical of the rhombohedral structure of LaCoO₃ were less pronounced upon addition of Pd, indicating an influence of Pd on the crystallization of the sample.

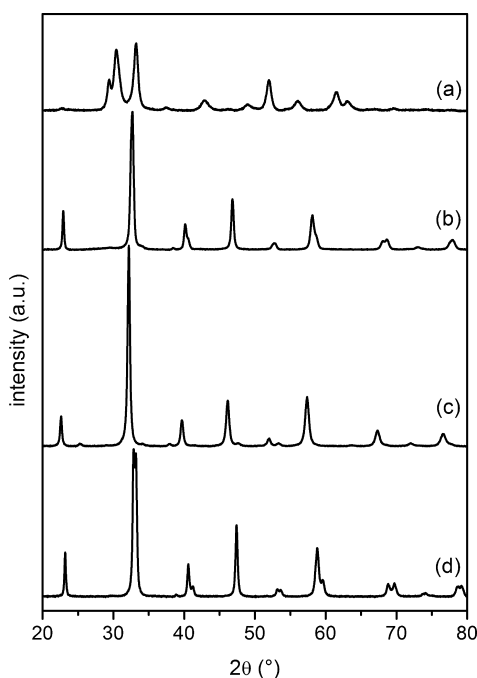


Figure 2. X-ray diffraction patterns of (a) $\text{Y(Fe,Pd)O}_3\text{-800}$, (b) La(Mn,Pd)O_3 , (c) La(Fe,Pd)O_3 , and (d) La(Co,Pd)O_3 .

3.2. X-ray Absorption Spectroscopy. The local environment of palladium in La(Mn,Pd)O_3 , La(Fe,Pd)O_3 , La(Co,Pd)O_3 , Y(Fe,Pd)O_3 , and $\text{Y(Fe,Pd)O}_3\text{-800}$ was studied by X-ray absorption spectroscopy (XAS). First, the XANES spectra of all samples were simulated under the assumption that, irrespective of the perovskite-type formulation, Pd substitutes the B-site cation and adopts its coordination environment. Simulation of the spectra was performed by adding a Pd atom in the coordination site of Mn, Fe, and Co using the crystal structures determined from the XRD data of Figure 2 and Table 1. The simulated XANES spectra shown in Figure 3a predict the white line of the Pd K-edge to exhibit a doublet that fingerprints Pd in distorted octahedral coordination in perovskite-type oxides.¹³ The difference with the white line of the PdO reference is obvious. The second derivative of the spectra is also shown in Figure 3b. In the case of the octahedral coordination, a clear signal appears ca. 20 eV above the Fermi energy that is absent in PdO in square planar coordination. This peak has been associated with shakeup processes involving $1s \rightarrow 5p$ transitions or multiple scattering.¹⁴ The occurrence of this feature in the samples prepared in this work was experimentally verified for La(Fe,Pd)O_3 and the spectrum of this sample is shown in Figure 4a. The white line of PdO in the form of particles exposed at the ABO_3 surface was shown to be clearly different and resembles the situation encountered for $\text{PdO}/\text{Al}_2\text{O}_3$ (Figure 4a), taken as characteristic of Pd^{2+} in square planar coordination (as in PdO) in a supported PdO catalyst. The difference between the two Pd coordination states is again evident from the second derivative of the experimental XANES spectra depicted in Figure 4b. The good agreement between simulated and experimental XANES data for La(Fe,Pd)O_3 is taken as proof of incorporation of Pd within the perovskite-type structure.

Figure 4a also shows the experimental XANES data of the other samples together with their second derivatives (Figure 4b). Clearly, the white line of La(Co,Pd)O_3 exhibited the same

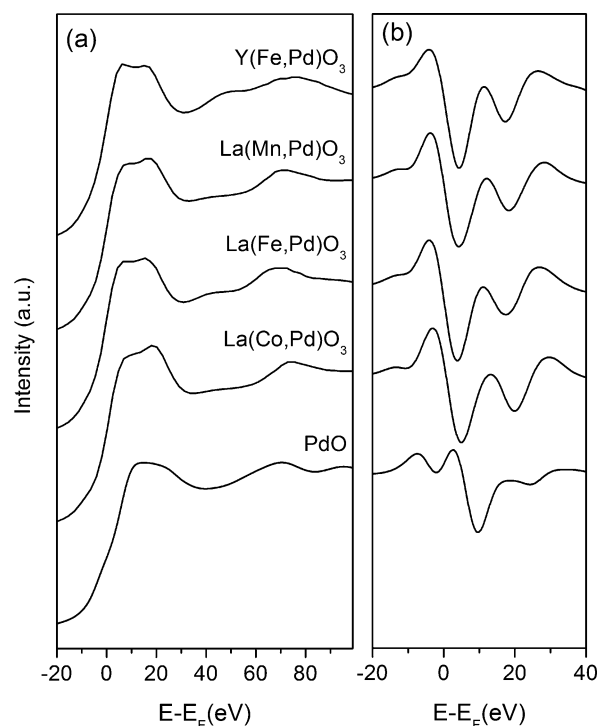


Figure 3. (a) Simulated XANES spectra of $\text{YFe}_{0.95}\text{Pd}_{0.05}\text{O}_3$, $\text{LaMn}_{0.95}\text{Pd}_{0.05}\text{O}_3$, $\text{LaFe}_{0.95}\text{Pd}_{0.05}\text{O}_3$, $\text{LaCo}_{0.95}\text{Pd}_{0.05}\text{O}_3$, and PdO and their (b) second derivatives. The energy scale is shifted relative to the position of the Fermi energy (E_F).

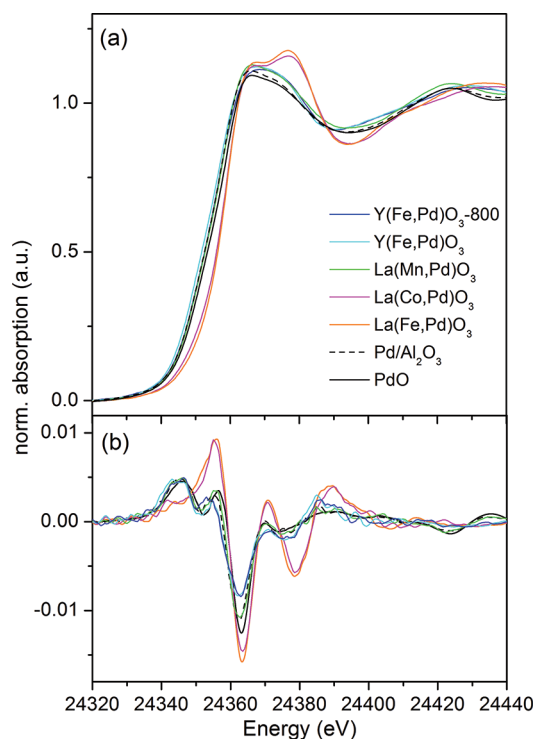


Figure 4. (a) Normalized XANES spectra of Y(Fe,Pd)O_3 , $\text{Y(Fe,Pd)O}_3\text{-800}$, La(Mn,Pd)O_3 , La(Fe,Pd)O_3 , La(Co,Pd)O_3 , $\text{Pd/Al}_2\text{O}_3$, and PdO with their (b) second derivatives.

doublet that is reflected in the peak at 20 eV above the Fermi energy in the second derivative. Hence, in this sample Pd

adopts the same coordination and probably oxidation state as in $\text{La}(\text{Fe,Pd})\text{O}_3$.

On the contrary, the white line of $\text{Y}(\text{Fe,Pd})\text{O}_{3-700}$, $\text{Y}(\text{Fe,Pd})\text{O}_{3-800}$, and $\text{La}(\text{Mn,Pd})\text{O}_3$ reflects a state of Pd that is more similar to that of Pd in $\text{PdO}/\text{Al}_2\text{O}_3$. Therefore, the XANES data indicate that in these samples Pd is most likely in square planar coordination characteristic of Pd^{2+} in PdO particles. It is evident from comparison of Figures 3a and 4a that the experimental XANES data of these samples contradict the simulated data predicting a similar Pd coordination for all samples. Therefore, either the solid solution between Pd and LaMnO_3 is not formed or Pd exhibits a different coordination environment providing a white line profile very similar to that of PdO . Pd was shown to occupy FeO_5 trigonal bipyramids in hexagonal $\text{YFe}_{1-x}\text{Pd}_x\text{O}_3$, but no XANES data have been reported.²¹ The spectrum in Figure 4a is also different from that of square planar Pd^{2+} adjacent to an oxygen vacancy in $\text{BaCe}_{1-x}\text{Pd}_x\text{O}_3$.¹⁹

The nonphase shift corrected Fourier transformed k^3 -weighted EXAFS spectra are shown in Figure 5 together with those of PdO and the Pd foil. All samples exhibit a first neighbor distance at 2.14 \AA ³² corresponding to Pd–O bonds well matching the spectrum of PdO . The FT spectra of $\text{La}(\text{Fe,Pd})\text{O}_3$, $\text{La}(\text{Co,Pd})\text{O}_3$, and $\text{Y}(\text{Fe,Pd})\text{O}_3$ do not display

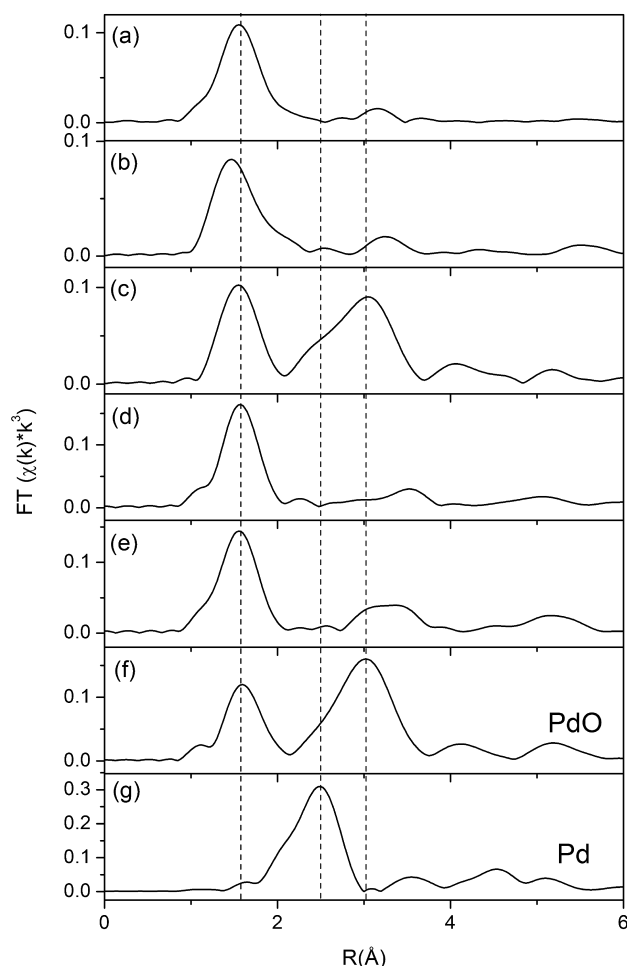


Figure 5. Radial distribution functions of the corresponding k^3 -weighted spectra of (a) $\text{Y}(\text{Fe,Pd})\text{O}_{3-700}$, (b) $\text{Y}(\text{Fe,Pd})\text{O}_{3-800}$, (c) $\text{La}(\text{Mn,Pd})\text{O}_3$, (d) $\text{La}(\text{Fe,Pd})\text{O}_3$, (e) $\text{La}(\text{Co,Pd})\text{O}_3$, (f) PdO , and (g) Pd.

additional defined features suggesting the fine dispersion of Pd. On the contrary, an important second Pd–O–Pd coordination shell is clearly observed at 3.42 \AA in the case of $\text{La}(\text{Mn,Pd})\text{O}_3$. Therefore, the EXAFS data confirm the formation of PdO -like particles on this sample in agreement with the Pd^{2+} oxidation state deduced from the XANES data. The well-defined PdO -like phase could explain the surface area loss after addition of Pd to LaMnO_3 (Table 1).

3.3. X-ray Photoelectron Spectroscopy. Information about the oxidation state of palladium at the near surface of the perovskite-type oxides was obtained by XPS. Figure 6 shows

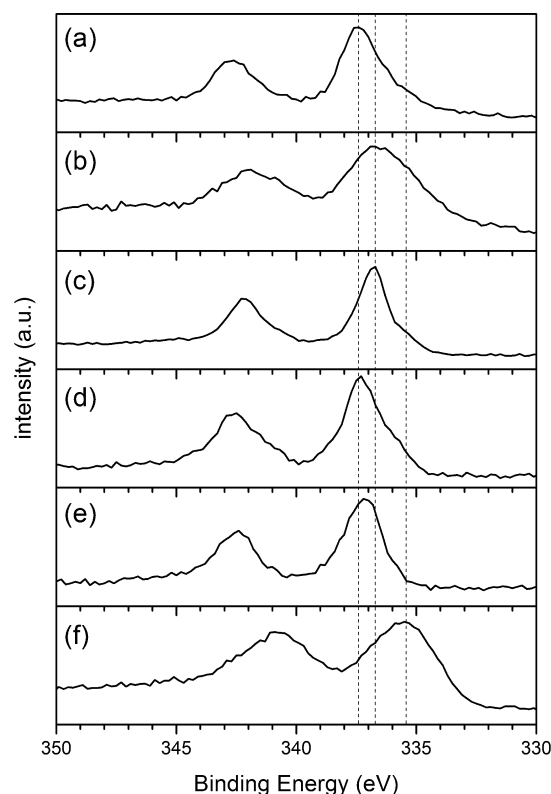


Figure 6. XPS analysis of the Pd $3d_{5/2}$ core level of (a) $\text{Y}(\text{Fe,Pd})\text{O}_{3-700}$, (b) $\text{Y}(\text{Fe,Pd})\text{O}_{3-800}$, (c) $\text{La}(\text{Mn,Pd})\text{O}_3$, (d) $\text{La}(\text{Fe,Pd})\text{O}_3$, (e) $\text{La}(\text{Co,Pd})\text{O}_3$, and (f) $\text{Pd}/\text{Al}_2\text{O}_3$.

the Pd $3d_{3/2}$ and $3d_{5/2}$ core level spectra of (a) $\text{Y}(\text{Fe,Pd})\text{O}_3$, (b) $\text{Y}(\text{Fe,Pd})\text{O}_{3-800}$, (c) $\text{La}(\text{Mn,Pd})\text{O}_3$, (d) $\text{La}(\text{Fe,Pd})\text{O}_3$, and (e) $\text{La}(\text{Co,Pd})\text{O}_3$. The spectrum of $\text{PdO}/\text{Al}_2\text{O}_3$ (Figure 6f) was used as a reference for palladium stabilized in the oxidation state +2 (PdO) that is confirmed by the XANES data (Figure 4a). The vertical lines in Figure 6 denote the reported ranges of the BE of Pd^0 ($\text{Pd} = 335.1\text{--}335.4 \text{ eV}$), Pd^{2+} ($\text{PdO} = 336.1\text{--}336.6 \text{ eV}$), and Pd^{4+} ($\text{PdO}_2 = 337.8\text{--}338.2 \text{ eV}$).³³

Starting from $\text{La}(\text{Fe,Pd})\text{O}_3$, the unusually high BE of Pd $3d_{5/2}$ at 337.36 eV and the symmetric photopeak (Figure 6d) indicate the existence of a dominant Pd^{n+} ($n > 2$) species. Pd replaces Fe at the B-site of LaFeO_3 where it could be stabilized in the oxidation state +3, and the high BE reflects the higher degree of ionicity of Pd and its stronger interaction with the LaFeO_3 lattice. Therefore, the state of Pd in $\text{La}(\text{Fe,Pd})\text{O}_3$ is homogeneous with respect to coordination environment and oxidation state. The XPS data of $\text{La}(\text{Fe,Pd})\text{O}_3$ can be taken as diagnostic of Pd in solid solution with the perovskite oxide.

The Pd 3d_{5/2} peak of La(Co,Pd)O₃ (337.17 eV, Figure 6e) indicates the same Pd state as in La(Fe,Pd)O₃ in agreement with previous reports^{7,34–36} and corroborates the XAS observation that in the two samples Pd is effectively in solid solution with the perovskite-type phase.

Figure 6a shows a narrow and symmetric Pd 3d_{5/2} photopeak for Y(Fe,Pd)O₃ that is centered at 337.45 eV (fwhm = 2.08 eV). It is tempting to associate the high BE with stabilized ionic Pdⁿ⁺ as in La(Fe,Pd)O₃ and therefore with the octahedral coordination of Pd. However, this does not seem feasible based on the hexagonal structure of the sample and from coordination arguments.²¹ The similar white line to that of PdO/Al₂O₃ (Figure 4a) encourages us to assume that palladium is stabilized in the square planar geometry (at least from the XANES viewpoint) but that it is not organized into PdO particles, because of the difference observed by XPS. The adopted coordination may be similar to that of the oxygen deficient BO₅ square pyramid observed in BaCe_{1-x}Pd_xO_{3-δ},^{12,19} therefore suggesting Pd²⁺ in a strong ionic environment. Calcination at 800 °C produces a sample exhibiting a peak at 336.58 eV (Figure 6b) that has a closer BE value to that of Pd²⁺ in PdO/Al₂O₃ (Figure 6f) indicating that Y(Fe,Pd)O₃-800 Pd is in a very similar state to that of dispersed PdO. The peak width (fwhm = 3.1 eV) and its asymmetry would indicate the presence of at least two Pd species, therefore including the one observed after calcination at 700 °C.

In support of the XAS data, La(Mn,Pd)O₃ exhibited a narrow Pd 3d_{5/2} peak at 336.79 eV that unambiguously verifies that palladium is in the oxidation state +2 (Figure 6c) and does not substitute Mn.

The BE values of the Pd 3d_{5/2} photopeaks of the various samples are in line with the surface Pd concentrations (Table 1). The quantitative data of the palladium content reflect the palladium concentration in the near surface region accessible to XPS. The absolute Pd content determined by ICP-OES is also provided. Although the Pd loadings are comparable, the values measured by XPS are low for La(Fe,Pd)O₃, La(Co,Pd)O₃, and Y(Fe,Pd)O₃. This information evokes the palladium depletion from the surface and its incorporation into the perovskite lattice. On the contrary, the higher Pd concentrations observed for La(Mn,Pd)O₃ and Y(Fe,Pd)O₃-800 suggest Pd enrichment at the near surface that can be associated with the formation of a clearly defined PdO phase. In the case of La(Mn,Pd)O₃, this confirms the XANES data and provides an explanation for the significant drop of specific surface area observed after addition of Pd to LaMnO₃ (Table 1). Calcination of Y(Fe,Pd)O₃ at 800 °C seems to force palladium to form PdO particles that together with the evolution of the hexagonal phase confirm the difficulty to insert Pd into YFeO₃.

3.4. Temperature Programmed Reduction (TPR). H₂-TPR is a useful complementary characterization method because it allows distinguishing between Pd incorporated within LaFeO₃ and Pd segregated on LaFeO₃, thus indicating the different availability of Pd.¹³ Reduction of the former species requires higher temperature than exposed PdO nanoparticles. Figure 7 shows the TPR profiles of all samples. The TPR profile of La(Fe,Pd)O₃ (Figure 7b) is characterized by a single peak at 270 °C. The character of the Pd species of La(Fe,Pd)O₃ in octahedral coordination observed by, for example, XPS and XAS indicates that this reduction event belongs to the reduction of Pd occupying the octahedral Fe sites.^{13,37,38}

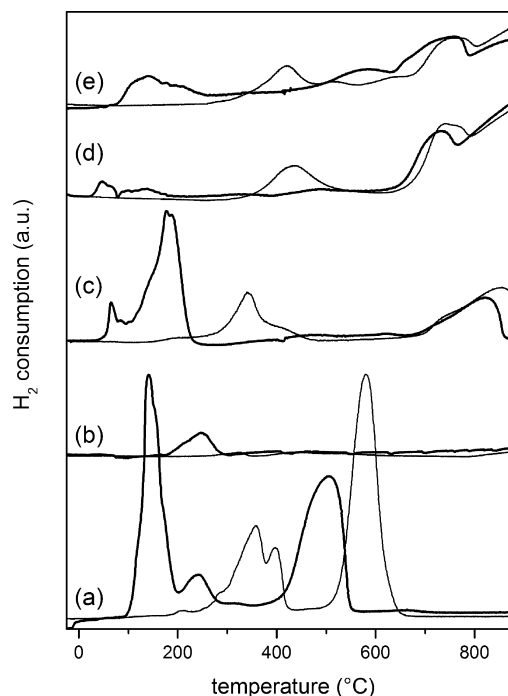


Figure 7. H₂-TPR profiles of (a) LaCoO₃/La(Co,Pd)O₃, (b) LaFeO₃/La(Fe,Pd)O₃, (c) LaMnO₃/La(Mn,Pd)O₃, (d) YFeO₃-800/Y(Fe,Pd)O₃-800, and (e) YFeO₃/Y(Fe,Pd)O₃. Thick lines represent Pd-containing samples.

Reduction of La(Mn,Pd)O₃ and La(Co,Pd)O₃ is complicated by the reducible perovskite structure. The main peak at 140 °C in the TPR profile of La(Co,Pd)O₃ (Figure 7a) is assigned to the reduction of LaCoO₃ to La₃CoO₈ and simultaneous reduction of PdO species to metallic palladium.^{35,39} The absence of any further reduction event at low temperature reveals that this Pd species corresponds to that providing the characteristic XANES profile and therefore of Pd incorporated in LaCoO₃. Since LaCoO₃ exhibits two H₂-consumption events at approximately 355 and 400 °C (LaCoO₃ → LaCoO_{2.67} and LaCoO_{2.67} → LaCoO_{2.5}),⁴⁰ the addition of Pd induces reduction of LaCoO₃ at lower temperature. Therefore, the lower reduction temperature than in La(Fe,Pd)O₃ for the same coordination state of Pd is caused by the reducibility of LaCoO₃. The further peaks observed in the TPR profile are associated with the subsequent Co₃O₄ → CoO reduction (180 °C), the reduction of La₃Co₃O₈ to La₂Co₂O₅ (240 °C), and of La₂Co₂O₅ to metallic cobalt and La₂O₃ (505 °C).^{35,39–42}

The reduction profile of LaMnO₃ is also characterized by reduction peaks at 340 °C, approximately 400 °C, and above 700 °C (Figure 7c), corresponding to the reduction sequence Mn⁴⁺ → Mn³⁺, Mn³⁺ → Mn²⁺.^{17,43,44} Similarly to La(Co,Pd)O₃, addition of Pd shifts the TPR profile to lower temperature. However, the weak but sharp low temperature peak at 65 °C is assigned to the reduction of Pd²⁺ to Pd⁰, whereas the envelope at 180 °C coincides with the reduction of Mn⁴⁺ to Mn³⁺ that is followed by the further reduction of Mn³⁺ to Mn²⁺ above 700 °C.^{17,45}

The TPR profiles of Y(Fe,Pd)O₃-800 and Y(Fe,Pd)O₃ shown in Figure 7d–e differ essentially in the low temperature peak observed at 45 and 140 °C, respectively. Since low temperature reduction is not observed in the case of the Pd-free samples, we assign both features to reduction of Pd²⁺ to

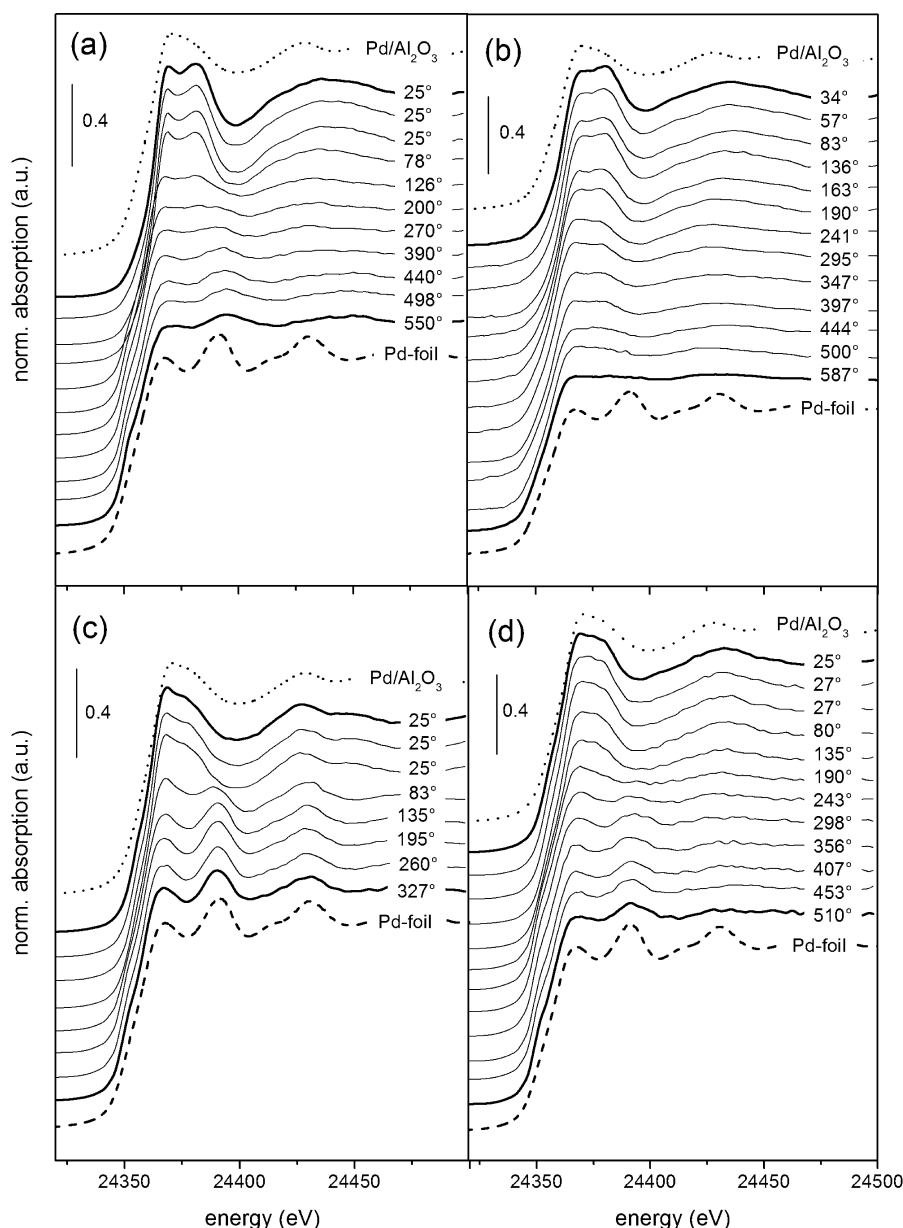


Figure 8. Normalized in situ XANES spectra of (a) $\text{La}(\text{Co,Pd})\text{O}_3$, (b) $\text{La}(\text{Fe,Pd})\text{O}_3$, (c) $\text{La}(\text{Mn,Pd})\text{O}_3$, and (d) $\text{Y}(\text{Fe,Pd})\text{O}_3$ during in situ reduction in 5 vol % H_2/He .

metallic Pd. However, the different temperature reveals the different nature of Pd in the two samples that already emerged from the XPS data of Figure 6. The width of the peak at 140 °C suggests slow reduction of PdO, which may be typical of large PdO particles or of palladium in strong interaction with the support. The peak at 45 °C reveals instead the presence of defined PdO-like particles. Further reduction peaks between 250 and 900 °C are attributed to reduction of Fe_2O_3 ((1) $\text{Fe}_2\text{O}_3 \rightarrow \text{Fe}_3\text{O}_4$, 250–400 °C, (2) $\text{Fe}_3\text{O}_4 \rightarrow \text{FeO}$, 350–900 °C, and (3) $\text{FeO} \rightarrow \text{Fe}$, above 700 °C)^{25,46–48} and of YFeO_3 to Fe and Y_2O_3 above 700 °C.⁴⁹ Participation of Fe_2O_3 present beside the hexagonal phase was confirmed by comparison with H_2 -TPR of Fe_2O_3 (not shown). Phase impurities of Y_2O_3 (Table 1) could also participate into the reduction profile since Y_2O_3 nanoparticles can reduce below 700 °C.^{50,51} This could be confirmed by the fact that reduction of the samples calcined at 800 °C, thus with improved crystallinity and larger Y_2O_3

particles, did not display the reduction peak at approximately 600 °C.

3.5. In Situ XANES during H_2 -TPR. The interpretation of the H_2 -TPR profiles of Pd-containing samples with respect to reduction of the Pd phase is supported by in situ XANES measurements. Figure 8a–d illustrates the results for $\text{La}(\text{Co,Pd})\text{O}_3$, $\text{La}(\text{Mn,Pd})\text{O}_3$, $\text{La}(\text{Fe,Pd})\text{O}_3$, and $\text{Y}(\text{Fe,Pd})\text{O}_3$. The initial state of Pd in the various samples is identical to that of Figure 3. The XANES spectra of $\text{PdO}/\text{Al}_2\text{O}_3$ and of the Pd foil, representative of Pd^{2+} and Pd^0 states, respectively, are also shown for clarity. During the H_2 -TPR, the white line of $\text{La}(\text{Fe,Pd})\text{O}_3$ and $\text{Y}(\text{Fe,Pd})\text{O}_3$ slowly and continuously attenuates, indicating the slow reduction of Pd, thus confirming the broad TPR reduction peaks observed in Figure 7. The final XANES spectrum of $\text{Y}(\text{Fe,Pd})\text{O}_3$ measured at approximately 500 °C reveals the characteristic features of palladium fcc particles. On the contrary, the spectrum of $\text{La}(\text{Fe,Pd})\text{O}_3$ reduced at approximately 600 °C is featureless.¹³ The small

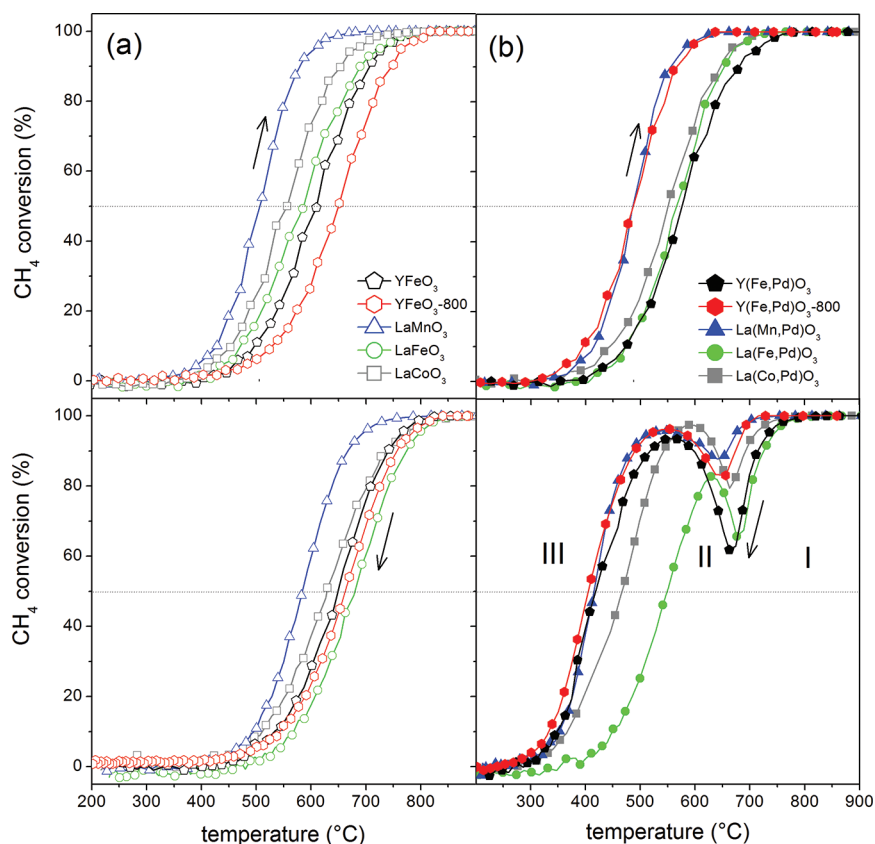


Figure 9. Light-off curves of methane oxidation during heating (\uparrow) and cooling (\downarrow) over (a) YFeO_3 , LaMnO_3 , LaFeO_3 , and LaCoO_3 (open symbols) and (b) Y(Fe,Pd)O_3 , La(Mn,Pd)O_3 , La(Fe,Pd)O_3 , and La(Co,Pd)O_3 (filled symbols).

size of the Pd particles formed by in situ reduction results in the damped spectrum of Figure 8b. The substantial difference between the two reduced states could be attributed to the ease of reduction of Pd coordinated to YFeO_3 compared to the La(Fe,Pd)O_3 solid solution.

La(Mn,Pd)O_3 (Figure 8c) and La(Co,Pd)O_3 (Figure 8a) show sharp reduction events at low temperature (25–80 °C and 80–200 °C, respectively) in agreement with the reduction peaks of Figure 7c,e. Reduction of Pd in the two samples is accomplished at 327 °C for La(Mn,Pd)O_3 and at 550 °C for La(Co,Pd)O_3 . The EXAFS oscillations characteristic of reduced Pd are more pronounced for La(Mn,Pd)O_3 . In this case, Pd particles are larger upon reduction than on La(Co,Pd)O_3 because reduction of PdO on LaMnO_3 occurs at lower temperature. On the contrary, La(Co,Pd)O_3 is able to stabilize incorporated palladium up to 140 °C (Figure 7e), thus diminishing the probability to observe particle sintering. Moreover, this difference also characterizes the reducibility of the existing PdO particles on La(Mn,Pd)O_3 .

3.6. Catalytic Activity. The effect of the different Pd states on the catalytic activity for methane oxidation was studied in the 200–900 °C temperature range during a full heating–cooling cycle. Activity was compared in terms of the temperature at which 50% CH_4 conversion is attained ($T_{50\%}$). The results for Pd-free and Pd-containing samples are shown in Figure 9a,b, respectively. The activity order of the Pd-free samples LaMnO_3 ($T_{50\%} = 505$ °C) > LaCoO_3 (555 °C) > LaFeO_3 (585 °C) > YFeO_3 (610 °C) > $\text{YFeO}_3\text{-800}$ (650 °C) remains similar during cooling, LaMnO_3 (585 °C) > LaCoO_3 (630 °C) > YFeO_3 (650 °C) > $\text{YFeO}_3\text{-800}$ (660 °C) > LaFeO_3 (680 °C). All catalysts lost activity after reaching 900 °C and

exhibited a hysteresis in the activity most likely because of the loss of specific surface area caused by exposure to higher temperature than that of calcination (700 °C). The loss is larger for LaMnO_3 , LaCoO_3 , and LaFeO_3 ($\Delta T_{50\%} = 80\text{--}95$ °C) than for YFeO_3 ($\Delta T_{50\%} = 40$ °C) and $\text{YFeO}_3\text{-800}$ ($\Delta T_{50\%} = 10$ °C). The $T_{50\%}$ of YFeO_3 is more affected than that of $\text{YFeO}_3\text{-800}$, since YFeO_3 experienced a larger loss of specific surface area upon heating above the calcination temperature and formation of the hexagonal phase (Figure 1).

Addition of Pd leaves the activity order in the heating segment unaltered. The $T_{50\%}$ values increase in the order La(Mn,Pd)O_3 ($T_{50\%} = 485$ °C) = $\text{Y(Fe,Pd)O}_3\text{-800}$ (485 °C) < La(Co,Pd)O_3 (550 °C) < La(Fe,Pd)O_3 (565 °C) < Y(Fe,Pd)O_3 (575 °C). The CH_4 conversion profiles in the cooling segment can be divided into three activity regions:⁵² region I (900 °C to ca. 660 °C), where activity drops; region II (ca. 660–540 °C), where activity increases again; and region III (ca. 540–200 °C), where catalytic activity finally vanishes. This behavior is typical of supported PdO catalysts.⁵³ The activity of the perovskite-type support dominates in the high temperature region I and the order of activity follows that of the Pd-free samples during cooling (Figure 9a). Under these conditions, Pd is most likely in the metallic state. This observation should be verified further using, for example, in situ XANES.⁵² Region II is typically associated with Pd reoxidation and redispersion, and the catalyst gains activity because PdO is the necessary active phase for methane oxidation.^{52,54} In region III, where Pd is mostly present as PdO, the activity changes in the order $\text{Y(Fe,Pd)O}_3\text{-800}$ ($T_{50\%} = 405$ °C) < La(Mn,Pd)O_3 (416 °C) \approx Y(Fe,Pd)O_3 (420 °C) < La(Co,Pd)O_3 (466 °C) < La(Fe,Pd)O_3 (550 °C). The activity of Y(Fe,Pd)O_3 , $\text{Y(Fe,Pd)O}_3\text{-800}$, and

La(Mn,Pd)O₃ improved significantly, thus confirming the presence of surface PdO on these samples. The observation of the hysteresis in methane oxidation activity at high temperature during the cooling segment, even in the samples where Pd is incorporated within the support lattice, suggests that Pd reduces above the PdO–Pd transition threshold.¹³ Upon reoxidation in region II, either partial reincorporation of Pd or complete restoration of the original structure may occur in La(Fe,Pd)O₃ and La(Co,Pd)O₃. This does not appear to be the case for Y(Fe,Pd)O₃. Clearly, PdO species reduce at high temperature. However, the improvement of activity demonstrated by the $T_{50\%}$ values of this sample indicates that exposure of the sample to higher temperature than for calcination under the reactants atmosphere most likely produces structural changes in YFeO₃ and in Pd that render the sample similar to Y(Fe,Pd)O₃-800. The likely improved crystallinity of YFeO₃ during reaction at high temperature as revealed by the XRD data of Figure 1 does not allow to regenerate the Pd species characterizing the initial state of the sample calcined at 700 °C.

4. DISCUSSION

Palladium can occupy the B-site of perovskite-structured materials and exhibits interesting redox properties that can be exploited to generate catalysts with peculiar catalytic performance. The data reported above clearly demonstrate that Pd can adopt different local environments depending on the nature of the perovskite-type oxide and on the crystal structure. We shall provide here a tentative structural interpretation of the reason.

Depending on the host matrix, the oxidation state of Pd varies between +2 and +3 and its coordination environment from square planar to octahedral. In the typical oxidation catalysts of the ABO₃ series (A = La, B = Mn, Fe, Co) where the coordination geometry of the B-site is octahedral (BO₆ octahedra), it is generally assumed that a doping element such as Pd adopts the same coordination state, at least within the paradigm of the substitution levels used for catalytic applications. LaPdO₃, BaCe_{1-x}Pd_xO₃, and YFe_{1-x}Pd_xO₃ are symptomatic of three different coordination environments and two oxidation states of Pd.^{12,14,21} In LaPdO₃, Pd adopted the unusual oxidation state +3 and octahedral coordination. Such a situation is not allowed in BaCeO₃, where Pd²⁺ enters the perovskite-type lattice in square planar coordination (BO₄) adjacent to an oxygen vacancy. In hexagonal YFeO₃, Pd occupies the trigonal pyramidal 5-fold coordination of the Fe cations but is still able to adopt oxidation state +2.

The characterization data presented in this work clearly show that in this specific series of perovskite-type oxides and irrespective of the fact that the same synthesis procedure has been applied, Pd is able to adopt the coordination state of the B-site in the case of Fe and Co. Therefore, it exhibits a higher oxidation state than the characteristic Pd²⁺ and a distorted octahedral coordination. On the contrary, with the same substitution level Pd segregates at the surface of LaMnO₃. Whether Pd can adopt the same coordination environment of the B-site can be tentatively rationalized on the base of ionic radii arguments and on the electronic structure of the cations considered in this work. Formation of the perovskite-like crystal structure can be predicted using the Goldschmidt tolerance factor, $t = (r_A + r_O) / \sqrt{2(r_B + r_O)}$, where r_A , r_B , and r_O are the ionic radii of the ions (A- and B-sites and oxygen). Perovskites are formed for $0.75 < t < 1$. Distortion of the BO₆ octahedra decreases the value of t from that of the ideal cubic unit cell ($t = 1$). The tolerance factor of the various samples was determined

considering the ionic radii by Shannon and Prewitt (Table 2).⁵⁵ All cations were assumed in the oxidation state +3 with the 6-

Table 2. Goldschmidt Tolerance Factors of the Perovskite-Type Catalysts and Ionic Radii^a

B ³⁺ , CN = 6									
spin ^b	Pd-free		A(B,Pd)O ₃	Pd ³⁺ , CN = 6	Pd ²⁺ , CN = 6	Pd ²⁺ , CN = 4			
	ABO ₃	<i>t</i>		<i>t</i>					
hs	LaFeO ₃	0.948	La(Fe,Pd)O ₃	0.945	0.943	0.948			
ls		1.000		0.995	0.992	0.998			
hs	LaMnO ₃	0.948	La(Mn,Pd)O ₃	0.945	0.943	0.948			
ls		0.984		0.979	0.977	0.982			
hs	LaCoO ₃	0.968	La(Co,Pd)O ₃	0.964	0.962	0.967			
ls		1.000		0.995	0.992	0.998			
<i>r</i> _B (pm) ^a	Pd ²⁺	Pd ³⁺	Mn ³⁺	Mn ⁴⁺	Fe ²⁺	Fe ³⁺	Co ²⁺	Co ³⁺	
CN = 4	64								
CN = 6	86	76	hs	65	78	65	75	61	
			ls	58	54	61	55	65	55

^aIonic radii taken from ref.⁵⁵ ^bhs= high spin; ls= low spin. *t* = tolerance factor. CN= coordination number.

fold B-site coordination, 12-fold A-site coordinated, and complete incorporation of palladium within the substituted samples (similarly to the simulated XANES data of Figure 3). Moreover, the spin state of the B-cation was selected high for Fe⁵⁶ and Mn⁵⁷ and low for Co.⁵⁸ The values reported in Table 2 show that *t* for LaMnO₃ is always lower than that of LaFeO₃ and LaCoO₃, thus already indicating structural differences with implications for B-site substitution. However, it is also clear from Table 2 that *t* cannot predict whether Pd substitutes the B-site cation in the perovskite-type structure with this substitution level.

Electroneutrality, that is, the sum of the charges of A and B cations in an ABO₃ structure which equals the total charge of oxygen anions, must also be satisfied in order to obtain a perovskite-type structure. Electroneutrality is achieved by charge distribution such as A¹⁺B⁵⁺O₃, A²⁺B⁴⁺O₃, or A³⁺B³⁺O₃. However, anionic or cationic vacancies are typically observed, the oxygen deficiency being rather common given the difficulty to insert interstitial oxygen in the perovskite-type structure. Reductive or oxidative nonstoichiometry can compensate the charge differences to satisfy electroneutrality.^{2,59} The difference between the oxidative nonstoichiometry of manganates (e.g., LaMnO₃, Mn^{3+/4+}) and the reductive nonstoichiometry of ferrates (Fe^{2+/3+}) and cobaltites (Co^{2+/3+}) may help to explain the observed tendency of Pd to adopt octahedral coordination in the latter and therefore to occupy the B-site position, which is not observed for LaMnO₃. Assuming that this is also the situation in the samples prepared in this work, it is considered that palladium can be hosted as Pd³⁺ ($r_{Pd3+} = 76$ pm) in LaFeO₃ ($r_{Fe2+,hs} = 78$ pm) and LaCoO₃ ($r_{Co2+,hs} = 75$ pm) because its ionic radius better matches that of the B-site cation. On the contrary, the oxidative nonstoichiometry of LaMnO₃ causes the formation of the Mn³⁺–Mn⁴⁺ pair with ionic radii that cannot be matched by the larger Pd³⁺. Rather, a square planar coordination of Pd in oxidation state +2 ($r_{Pd2+} = 64$ pm) would be preferred based on this argument. As a consequence, either Pd adopts a coordination similar to that described in BaCeO₃¹² or is forced into the square planar coordination of PdO to form particles at the surface of LaMnO₃. However, BaCeO₃ was

shown to exhibit oxygen deficiency. Hence, we consider that palladium prefers a square planar coordination in LaMnO_3 with formation of PdO.

In the hexagonal structure, the A-site cation is sevenfold coordinated, and the B-site cation possesses fivefold coordination. In YFeO_3 , Fe^{3+} is in trigonal bipyramidal coordination (BO_5). Pd^{2+} fits into this geometry and stabilizes the hexagonal structure versus the high-temperature perovskite structure.²¹ The characterization data indicate that Y(Fe,Pd)O_3 and Y(Fe,Pd)O_{3-800} possess very similar XANES white lines and TPR profiles but are clearly different with respect to their oxidation state determined by XPS. Therefore, while the short-range coordination environment of Pd may be very similar, the degree of interaction with YFeO_3 varies, most likely depending on the crystallinity of the support oxide. Calcination as low as 700 °C seems to confer Pd a stronger ionic environment, which is probably that corresponding to fivefold coordinated Pd^{2+} .²¹ Thus, the XANES profiles of the two samples calcined at different temperatures appear similar. Calcination at 800 °C results in improved crystallinity of YFeO_3 and a Pd state similar to that of PdO, thus revealing the formation of PdO particles. Therefore, we do not have evidence for incorporation of Pd in fivefold coordination at this temperature but rather of a bulk PdO phase on the surface of hexagonal YFeO_3 .

The observed palladium states differently affected the catalytic activity for CH_4 oxidation of the La(B,Pd)O_3 ($\text{B} = \text{Mn, Fe, Co}$) series and Y(Fe,Pd)O_3 samples. Catalysts with Pd predominantly in the form of PdO particles reveal highest catalytic activity (La(Mn,Pd)O_3 and Y(Fe,Pd)O_{3-800} , Pd^{2+} , square planar) because supported PdO nanoparticles are highly active for methane oxidation. On the contrary, catalysts with incorporated (La(Fe,Pd)O_3 , La(Co,Pd)O_3 , Pd^{3+} , octahedral) or strongly bound Pd (Y(Fe,Pd)O_3 , Pd^{2+} , square planar) show lowest catalytic activity probably because Pd is not accessible to methane. Therefore, the high temperature activity is basically dictated by the perovskite structure.

Oxidation reactions on perovskite-type oxides can be influenced by different oxygen species. Low temperature oxidation ($T < 400$ °C) is considered a suprafacial process, where adsorbed oxygen provided by the gas phase is used as the oxidant and the reaction may follow the Eley–Rideal mechanism.⁵ Therefore, catalytic activity can depend on structural defects. CO oxidation is a typical suprafacial reaction on perovskite-structured catalysts where oxygen vacancies play a major role.¹⁹ With increasing temperature the surface coverage of molecular oxygen decreases and the mobility of lattice oxygen increases. Therefore, at higher temperature the reactions become intrafacial processes, where the oxygen provided by the catalyst lattice plays a major role and the rate of oxygen incorporation into the lattice is faster than its consumption.^{5,60,61} The intrafacial process typically follows the Mars–van Krevelen mechanism involving consumption of lattice oxygen and its backfilling from gas phase oxygen. Methane oxidation on perovskite-type catalysts is an example of an intrafacial process where the increased oxygen mobility dominates catalytic activity. We can use this approach to follow the effect of Pd addition on catalytic activity. Therefore, if Pd is incorporated within the perovskite-type structure, it should not affect activity since CH_4 oxidation occurs at high temperature. On the contrary, the presence of segregated Pd(O) would improve activity for CH_4 oxidation with respect to the mixed oxide, because PdO particles are generally more active at low temperature than a Pd-free perovskite-type catalyst.⁶² In line

with the characterization data, the better activity demonstrated by La(Mn,Pd)O_3 and Y(Fe,Pd)O_{3-800} can be attributed to the presence of Pd^{2+} exposed in the form of PdO-like particles. The low temperature catalytic activity of these two samples is also consistent with their ease of reduction observed in H_2 -TPR experiments, pointing to the presence of readily available PdO particles.

The structural difference between the samples becomes also evident after reaching the maximum reaction temperature of 900 °C and during the subsequent cooling. The CH_4 conversion profiles of the Pd-containing samples show typical hysteresis and an activity loss. The activity minimum is attributed to the formation of metallic Pd at temperatures above the PdO–Pd equilibrium threshold. The PdO–Pd decomposition temperature is different for the samples and depends on the possible stabilization of the PdO species by the perovskite-type lattice. Bulk-like PdO decomposes at low temperature and consequently forms larger Pd particles due to sintering compared to Pd in solid solution that emerges gradually and at higher temperature from the perovskite-type support. During cooling, metallic palladium reoxidizes either partly or completely below the PdO–Pd threshold, depending on the size of formed metallic Pd particles. This explains the observed different “reactivation” levels between 530 and 590 °C. Additionally, when enabled by the structure (i.e., LaFeO_3 and LaCoO_3), Pd can be reincorporated upon further cooling. This situation accounts for the lower catalytic activity observed for La(Fe,Pd)O_3 and La(Co,Pd)O_3 .

5. CONCLUSIONS

A series of palladium doped perovskite-type oxides of nominal formula $\text{LaB}_{1-x}\text{Pd}_x\text{O}_{3\pm\delta}$ ($\text{B} = \text{Co, Fe, Mn}$, denoted as La(B,Pd)O_3) and $\text{YFe}_{1-x}\text{Pd}_x\text{O}_{3\pm\delta}$ have been synthesized by the amorphous citrate method. Characterization data of XPS, XANES, EXAFS, and H_2 -TPR reveal that at least two Pd species populate the various samples and that their distribution is dependent on the catalyst formulation. The two identified species are supported PdO-like particles and well-dispersed octahedral Pd–O species substituting the B-site cation. In the case of perovskite-type catalysts, the latter species was found for Fe and Co B-site cations, in agreement with the reported self-regenerative property of $\text{LaFe}_{0.95}\text{Pd}_{0.05}\text{O}_3$. For Mn as the B-site cation, a widely reported methane oxidation catalyst, Pd deposits in the form of PdO particles on LaMnO_3 . The influence of the palladium state has been related to the catalytic activity for methane oxidation in the temperature range 200–900 °C. The activity of the catalysts strongly depends on the state of Pd, since typically PdO is considered the active phase for the reaction. Therefore, exposed PdO particles make La(Mn,Pd)O_3 more active than La(Co,Pd)O_3 and La(Fe,Pd)O_3 . The different behavior of Pd with respect to the perovskite-type formulation is explained in terms of ionic radii arguments and of the different redox properties of LaMnO_3 vs LaFeO_3 / LaCoO_3 .

In the case of Y(Fe,Pd)O_3 , the state of Pd appears to be calcination temperature dependent. When YFeO_3 is largely still amorphous, a strong interaction between Pd and the support is observed that is similar in terms of influence on catalytic activity to that exhibited by La(Fe,Pd)O_3 and La(Co,Pd)O_3 . The improved crystallinity of YFeO_3 after higher calcination temperature forces Pd to form PdO particles, which strongly promotes catalytic activity. The data reveal that YFeO_3 may be a promising support for Pd for methane oxidation.

The data also suggest that the formation of a solid solution between Pd and common perovskite-type oxidation catalysts needs to be carefully ascertained and strongly depends on the composition of the perovskite oxide.

AUTHOR INFORMATION

Corresponding Author

*E-mail: davide.ferri@empa.ch. Phone: +41 58 765 4609. Fax: +41 58 765 4041.

Present Address

[†]Hug Engineering AG, Im Geren, CH-8352 Elsau, Switzerland

Notes

The authors declare no competing financial interest.

ACKNOWLEDGMENTS

The authors kindly acknowledge Empa and the Swiss National Science Foundation (National Research Program NRP 62 Smart Materials, Project No. 406240-126127) for financial support and the Swiss Light Source (Villigen, Switzerland) and Hasylab (DESY, Hamburg, Germany) for beamtime allocation.

DEDICATION

[†]The manuscript is dedicated to Dr. P. Hug who passed away on November 24, 2011.

REFERENCES

- Peña-Martínez, J.; Marrero-López, D.; Ruiz-Morales, J. C.; Buergler, B. E.; Núñez, P.; Gauckler, L. J. *J. Power Sources* **2006**, *159*, 914.
- Pena, M. A.; Fierro, J. L. G. *Chem. Rev.* **2001**, *101*, 1981.
- Royer, S.; Duprez, D. *ChemCatChem* **2011**, *3*, 24.
- Kim, H. G.; Becker, O. S.; Jang, J. S.; Ji, S. M.; Borse, P. H.; Lee, J. S. *J. Sol. State Chem.* **2006**, *179*, 1214.
- Tejuca, L. G.; Fierro, J. L. G.; Tascón, J. M. D.; D.D. Eley, H. P.; Paul, B. W. *Adv. Catal.* **1989**, *36*, 237.
- Robert, R.; Aguirre, M. H.; Bocher, L.; Trottmann, M.; Heiroth, S.; Lippert, T.; Döbeli, M.; Weidenkaff, A. *Solid State Sci.* **2008**, *10*, 502.
- Nishihata, Y.; Mizuki, J.; Akao, T.; Tanaka, H.; Uenishi, M.; Kimura, M.; Okamoto, T.; Hamada, N. *Nature* **2002**, *418*, 164.
- Tanaka, H.; Taniguchi, M.; Uenishi, M.; Kajita, N.; Tan, I.; Nishihata, Y.; Mizuki, J.; Narita, K.; Kimura, M.; Kaneko, K. *Angew. Chem., Int. Ed.* **2006**, *45*, 5998.
- Goldwasser, M. R.; Rivas, M. E.; Pietri, E.; Pérez-Zurita, M. J.; Cubeiro, M. L.; Gengembre, L.; Leclercq, L.; Leclercq, G. *Appl. Catal., A* **2003**, *255*, 45.
- Navarro, R. M.; Alvarez-Galvan, M. C.; Villoria, J. A.; González-Jiménez, I. D.; Rosa, F.; Fierro, J. L. G. *Appl. Catal., B* **2007**, *73*, 247.
- Uenishi, M.; Taniguchi, M.; Tanaka, H.; Kimura, M.; Nishihata, Y.; Mizuki, J.; Kobayashi, T. *Appl. Catal., B* **2005**, *57*, 267.
- Li, J.; Singh, U. G.; Bennett, J. W.; Page, K.; Weaver, J. C.; Zhang, J. P.; Proffen, T.; Rappe, A. M.; Scott, S.; Seshadri, R. *Chem. Mater.* **2007**, *19*, 1418.
- Eyssler, A.; Mandaliyev, P.; Winkler, A.; Hug, P.; Safonova, O.; Figi, R.; Weidenkaff, A.; Ferri, D. *J. Phys. Chem. B* **2010**, *114*, 4584.
- Kim, S. J.; Lemaux, S.; Demezeau, G.; Kim, J. Y.; Choy, J. H. J. *J. Mater. Chem.* **2002**, *12*, 995.
- Wei, X.; Hug, P.; Figi, R.; Trottmann, M.; Weidenkaff, A.; Ferri, D. *Appl. Catal., B* **2010**, *94*, 27.
- Cimino, S.; Casaletto, M. P.; Lisi, L.; Russo, G. *Appl. Catal., A* **2007**, *327*, 238.
- Giebler, L.; Kiessling, D.; Wendt, G. *Chem. Eng. Technol.* **2007**, *30*, 889.
- Kimura, M.; uemura, K.; Nagai, T.; Niwa, Y.; Inada, Y.; Nomura, M. *J. Phys.: Conf. Ser.* **2009**, *190*, 012163.
- Ouyang, X.; Scott, S. L. *J. Catal.* **2010**, *273*, 83.
- Kizaki, H.; Kusakabe, K.; Nogami, S.; Katayama-Yoshida, H. *Appl. Phys. Express* **2008**, *1*, 104001.
- Li, J.; Singh, U. G.; Schladt, T. D.; Stalick, J. K.; Scott, S. L.; Seshadri, R. *Chem. Mater.* **2008**, *20*, 6567.
- Tejuca, L. G.; Fierro, J. L. G.; Tascón, J. M. D. *Adv. Catal.* **1989**, *36*, 237.
- Baythoun, M. S. G.; Sale, F. R. *J. Mater. Sci.* **1982**, *17*, 2757.
- Grunwaldt, J. D.; Caravati, M.; Hannemann, S.; Baiker, A. *Phys. Chem. Chem. Phys.* **2004**, *6*, 3037.
- SanthoshKumar, M.; Eyssler, A.; Hug, P.; vanVegten, N.; Baiker, A.; Weidenkaff, A.; Ferri, D. *Appl. Catal., B* **2010**, *94*, 77.
- Ravel, B.; Newville, M. *J. Synchrotron. Radiat.* **2005**, *12*, 537.
- Yamaguchi, O.; Takemura, H.; Yamashita, M. *J. Electrochem. Soc.* **1991**, *138*, 1492.
- Ayyub, P.; Multani, M. S.; Gurjar, A. *Mater. Lett.* **1983**, *2*, 122.
- Cheetham, A. K.; Rao, C. N. R.; Vogt, T. *J. Solid State Chem.* **1996**, *126*, 337.
- Thornton, G.; Tofield, B. C.; Hewat, A. W. *J. Solid State Chem.* **1986**, *61*, 301.
- Taguchi, H.; Masunaga, Y.; Hirota, K.; Yamaguchi, O. *Mater. Res. Bull.* **2005**, *40*, 773.
- Waser, J.; Levy, H. A.; Peterson, S. W. *Acta Crystallogr.* **1953**, *6*, 661.
- Moulder, J. F.; Stickle, W. F.; Sobol, P. E.; Bomben, K. D. *Handbook of X-Ray Photoelectron Spectroscopy*; Perkin-Elmer Corp.: Eden Prairie, MN, 1992.
- MondragonRodriguez, G. C.; Ochrombel, R.; Saruhan, B. *J. Eur. Ceram. Soc.* **2008**, *28*, 2611.
- Dacquín, J. P.; Dujardin, C.; Granger, P. *J. Catal.* **2008**, *253*, 37.
- Giraudon, J. M.; Elhachimi, A.; Leclercq, G. *Appl. Catal., B* **2008**, *84*, 251.
- Tanaka, H.; Tan, I.; Uenishi, M.; Taniguchi, M.; Kimura, M.; Nishihata, Y.; Mizuki, J. *J. Alloys Comp.* **2006**, *408–412*, 1071.
- Zhou, K.; Chen, H.; Tian, Q.; Hao, Z.; Shen, D.; Xu, X. *J. Mol. Catal. A: Chem.* **2002**, *189*, 225.
- Sartipi, S.; Khodadadi, A. A.; Mortazavi, Y. *Appl. Catal., B* **2008**, *83*, 214.
- Chiarello, G. L.; Ferri, D.; Grunwaldt, J. D.; Forni, L.; Baiker, A. *J. Catal.* **2007**, *252*, 127.
- Dacquín, J. P.; Lancelot, C.; Dujardin, C.; Da Costa, P.; Djega-Mariadassou, G.; Beaunier, P.; Kaliaguine, S.; Vaudreuil, S.; Royer, S.; Granger, P. *Appl. Catal., B* **2009**, *91*, 596.
- Huang, L.; Bassir, M.; Kaliaguine, S. *Appl. Surf. Sci.* **2005**, *243*, 360.
- Patcas, F.; Buciuman, F. C.; Zsako, J. *Thermochim. Acta* **2000**, *360*, 71.
- Fierro, J. L. G.; Tascón, J. M. D.; Tejuca, L. G. *J. Catal.* **1984**, *89*, 209.
- Stephan, K.; Hackenberger, M.; Kieffling, D.; Richter, F.; Wendt, G. *Chem. Eng. Technol.* **2002**, *25*, 559.
- Munteanu, G.; Ilieva, L.; Andreeva, D. *Thermochim. Acta* **1997**, *291*, 171.
- Zielinski, J.; Zglinicka, I.; Znak, L.; Kaszkur, Z. *Appl. Catal., A* **2010**, *381*, 191.
- Khan, A.; Smirniotis, P. G. *J. Mol. Catal. A: Chem.* **2008**, *280*, 43.
- Carreiro, L.; Qian, Y. T.; Kershaw, R.; Dwight, K.; Wold, A. *Mater. Res. Bull.* **1985**, *20*, 619.
- Sun, G. B.; Hidajat, K.; Wu, X. S.; Kawi, S. *Appl. Catal., B* **2008**, *81*, 303.
- Costa, L. O. O.; Silva, A. M.; Borges, L. E. P.; Mattos, L. V.; Noronha, F. B. *Catal. Today* **2008**, *138*, 147.
- SanthoshKumar, M.; Aguirre, M. H.; Weidenkaff, A.; Ferri, D. *J. Phys. Chem. C* **2010**, *114*, 9439.
- Farrauto, R. J.; Hobson, M. C.; Kennelly, T.; Waterman, E. M. *Appl. Catal., A* **1992**, *81*, 227.
- Burch, R.; Urbano, F. J. *Appl. Catal., A* **1995**, *124*, 121.
- Shannon, R. D.; Prewitt, C. T. *Acta Crystallogr.* **1969**, *B25*, 925.

- (56) Abbate, M.; deGroot, F. M. F.; Fuggle, J. C.; Fujimori, A.; Strebel, O.; Lopez, F.; Domke, M.; Kaindl, G.; Sawatzky, G. A.; Takano, M.; Takeda, Y.; Eisaki, H.; Uchida, S. *Phys. Rev. B* **1992**, *46*, 4511.
- (57) Goodenough, J. B.; Gschneidner, K. A.; Bünzli, J. C. G.; Pecharsky, V. K. In *Handbook on the Physics and Chemistry of Rare Earths*; Elsevier: 2003; Vol. 33, p 249.
- (58) Parkash, O.; Ganguly, P.; Rao, G. R.; Rao, C. N. R.; Rajoria, D. S.; Bhide, V. G. *Mater. Res. Bull.* **1974**, *9*, 1173.
- (59) Smyth, D. M. *Annu. Rev. Mater. Sci.* **1985**, *15*, 329.
- (60) Voorhoeve, R. J. H.; Remeika, J. P.; Trimble, L. E. *Ann. N.Y. Acad. Sci.* **1976**, *272*, 3.
- (61) Voorhoeve, R. J. H. *Advanced Materials in Catalysis*; Academic Press: New York, 1977.
- (62) Ciuparu, D.; Lyubovsky, M. R.; Altman, E.; Pfefferle, L. D.; Datye, A. *Catal. Rev.: Sci. Eng.* **2002**, *44*, 593.
- (63) Closset, N.; vanDoorn, R.; Kruidhof, H.; Boeijsma, J. *Powder Diffr.* **1996**, *11*, 31.